

Giant chirality-induced spin polarization in twisted transition metal dichalcogenides

Guido Menichetti,^{1,*} Lorenzo Cavicchi,² Leonardo Lucchesi,^{1,3} Fabio Taddei,^{4,2} Giuseppe Iannaccone,³ Pablo Jarillo-Herrero,⁵ Claudia Felser,⁶ Frank H. L. Koppens,^{7,8} and Marco Polini^{1,7}

¹Dipartimento di Fisica dell'Università di Pisa, Largo Bruno Pontecorvo 3, I-56127 Pisa, Italy

²Scuola Normale Superiore, Piazza dei Cavalieri 7, I-56126 Pisa, Italy

³Dipartimento di Ingegneria dell'Informazione dell'Università di Pisa, Via Girolamo Caruso 16, I-56122 Pisa, Italy

⁴NEST, Istituto Nanoscienze-CNR, Piazza S. Silvestro 12, I-56126 Pisa, Italy

⁵Department of Physics, Massachusetts Institute of Technology, Cambridge, Massachusetts, USA

⁶Max Planck Institute for Chemical Physics of Solids, Nöthnitzer Str. 40, Dresden 01187, Germany

⁷ICFO-Institut de Ciències Fotòniques, The Barcelona Institute of Science and Technology, Av. Carl Friedrich Gauss 3, 08860 Castelldefels (Barcelona), Spain

⁸ICREA-Institució Catalana de Recerca i Estudis Avançats, Passeig de Lluís Companys 23, 08010 Barcelona, Spain

(Dated: January 24, 2024)

Chirality-induced spin selectivity (CISS) is an effect that has recently attracted a great deal of attention in chiral chemistry and that remains to be understood. In the CISS effect, electrons passing through chiral molecules acquire a large degree of spin polarization. In this work we study the case of atomically-thin chiral crystals created by van der Waals assembly. We show that this effect can be spectacularly large in systems containing just two monolayers, provided they are spin-orbit coupled. Its origin stems from the combined effects of structural chirality and *spin-flipping* spin-orbit coupling. We present detailed calculations for twisted homobilayer transition metal dichalcogenides, showing that the chirality-induced spin polarization can be giant, e.g. easily exceeding 50% for MoTe₂. Our results clearly indicate that twisted quantum materials can operate as a fully tunable platform for the study and control of the CISS effect in condensed matter physics and chiral chemistry.

Introduction.—In 1999, a team led by R. Naaman recognized that films made from chiral organic molecules scatter polarized electrons asymmetrically [1]. Spin polarization induced by chirality is an effect now universally known as chirality-induced spin selectivity (CISS) effect [2–6]. Almost ten years later, Rosenberg et al. [7] demonstrated that a polarized spin can induce an enantiospecific chemical process. It is now widely accepted [2–6] that the CISS effect has profound implications on asymmetric chemistry. Chiral molecules and, more in general, chiral materials [8] and bulk chiral crystals [9] can act as spin polarizers and filters and therefore influence processes associated with electron transfer, electron transport, and bond polarization through chiral structures.

To the best of our knowledge, though, a microscopic understanding of the molecular CISS effect is still lacking (for a recent summary we refer the reader to Ref. [10]). In particular, the role of spin-orbit coupling [10], geometric phases [11], electron correlations [12], electron-phonon coupling [13], dissipation [14], and the interactions between chiral molecules and/or chiral and magnetic substrates are not understood. This confusion on its microscopic origin limits the use of CISS in applications and makes it challenging to enhance it.

The point we want to raise in this work is that a thorough microscopic understanding of the CISS effect calls for a fully tunable platform where the dependence of the effect on a multitude of control parameters can be studied, both experimentally and theoretically. As we will demonstrate below, we believe that moiré superlat-

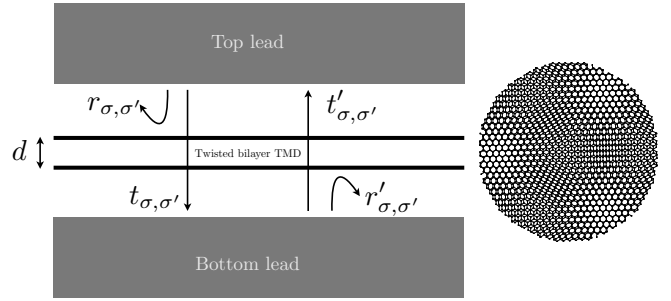


FIG. 1. Sketch of the two-terminal setup we have studied in this work. A twisted homobilayer TMD, developing along the \hat{x} - \hat{y} plane, is contacted by two semi-infinite leads (denoted by grey-shaded areas). The spatial separation between the two TMD layers in the vertical \hat{z} direction is d . The twist between the two layers is achieved by a counter-clockwise rotation of the top layer with respect to the bottom one by an angle θ . The resulting moiré lattice is plotted on the right. Black arrows show the spin-resolved reflection, $r_{\sigma,\sigma'}$, $r'_{\sigma,\sigma'}$, and transmission, $t_{\sigma,\sigma'}$, $t'_{\sigma,\sigma'}$, components of the scattering matrix S reported in Eq. (1).

tices obtained by twisting atomically-thin crystals with respect to each other [15–17] represent such a platform. Despite the great deal of interest that these systems have attracted since the discovery of superconductivity [18] and correlated insulating states [19] in twisted bilayer graphene (TBG) [20–28], very few studies have highlighted the fact that these systems are naturally chiral materials akin to “giant chiral molecules”. The only qualitative difference between chiral molecules and twisted

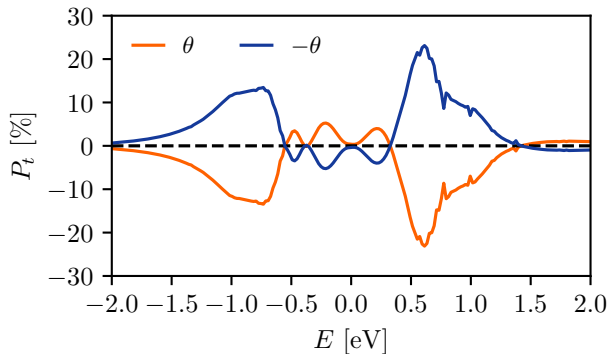


FIG. 2. (Color online) Numerical results for the energy dependence of the spin polarization $P_t = P_t(E)$, as defined in Eq. (5), of electrons transmitted from the top to the bottom lead. The calculated spin polarization has opposite sign for θ (orange curve) and $-\theta$ (blue curve). In the non-chiral (untwisted, $\theta = 0$) case, the spin polarization P_t vanishes (black dashed line). Results in this plot refer to parameters for twisted homobilayer MoTe_2 [49], $\theta = 6.01^\circ$, $\lambda_0 = 220$ meV, and $\lambda_{\text{BR}} = 0$.

quasi-two-dimensional (2D) materials is that the latter have (a nearly exact) Bloch translational invariance.

The fact that twisted materials are chiral is not a mere mathematical statement but has experimental implications e.g. on the interaction between these materials and light. For example, natural optical activity [29], a hallmark of chiral materials, was experimentally discovered [30] in TBG at large twist angles well before exotic states of matter were found at the magic angle [18, 19]. TBG exhibits remarkably large circular dichroism [30, 31], up to a factor 100 stronger than for a layer of chiral molecules of similar thickness.

In this work, we demonstrate that the interplay between spin-orbit coupling (SOC) and chirality in twisted quantum materials gives rise to a giant CISS effect, *even for just two twisted monolayers*. More precisely, we consider a family of twisted moiré superlattices which are known to display strong SOC. These are twisted homobilayer transition metal dichalcogenides (TMDs) [32] such as twisted MoTe_2 , which is currently attracting a great deal of attention because of the experimental discovery [33–36] of fractional Chern insulating states in zero magnetic field. These systems offer a wide range of tunable parameters, such as carrier density (which can be changed via e.g. the electrical field effect), twist angle (which can be changed at will, thereby inducing dramatic changes in the Bloch bands of these crystals), and more conventional ones, such as temperature and applied magnetic fields. Our interest here is on the study of the interplay between chiral orbital motion, spin-orbit coupling, and the spin degree of freedom. Quantifying the role of electron-electron interactions (e.g. exchange interactions [37]), which are strong in moiré materials, and

quantum geometry [38–40] is well beyond the scope of the present work and is left for future work.

Setup and scattering matrix approach to the CISS effect.—In order to numerically extract information about the CISS effect in twisted homobilayer TMDs, we utilize the setup depicted in Fig. 1. It consists of a twisted homobilayer TMD contacted by two leads. One can inject carriers from the top lead, for example, which, after tunneling through the strongly spin-orbit coupled twisted homobilayer TMD, will be extracted from the bottom layer. As we will discuss momentarily, the reciprocity theorem [41] forbids the observation of a spin-polarized current through a standard linear-response magnetoresistance measurement in a two-terminal setup [42]. Nevertheless, the spin-polarized nature of electron scattering in our chiral van der Waals heterostructure can be detected through a spin-resolved scattering matrix approach [43–46].

The top and bottom leads in Fig. 1 offer asymptotic propagating states. We introduce: i) $\psi_{\text{T},\sigma}^{\text{out}}$ ($\psi_{\text{B},\sigma}^{\text{out}}$) as the asymptotic wave-function for electrons with spin $\sigma = \uparrow, \downarrow$, which are scattered out of the twisted homobilayer TMD into the top (bottom) lead; ii) $\psi_{\text{T},\sigma'}^{\text{in}}$ ($\psi_{\text{B},\sigma'}^{\text{in}}$) as the asymptotic wave-function for electrons with spin $\sigma' = \uparrow, \downarrow$, which are injected from the top (bottom) lead into the twisted homobilayer TMD. The latter can be viewed as a scatterer, whose transport properties are completely defined by its spin-resolved scattering matrix $S_{\sigma,\sigma'}$ [43]:

$$\begin{pmatrix} \psi_{\text{T},\sigma}^{\text{out}} \\ \psi_{\text{B},\sigma}^{\text{out}} \end{pmatrix} = \sum_{\sigma'=\uparrow,\downarrow} S_{\sigma,\sigma'} \begin{pmatrix} \psi_{\text{T},\sigma'}^{\text{in}} \\ \psi_{\text{B},\sigma'}^{\text{in}} \end{pmatrix}, \quad (1)$$

where

$$S_{\sigma,\sigma'} \equiv \begin{pmatrix} r_{\sigma,\sigma'} & t'_{\sigma,\sigma'} \\ t_{\sigma,\sigma'} & r'_{\sigma,\sigma'} \end{pmatrix}. \quad (2)$$

Here, $t_{\sigma,\sigma'}, r_{\sigma,\sigma'} (t'_{\sigma,\sigma'}, r'_{\sigma,\sigma'})$ are the spin-resolved transmission and reflection amplitudes of electrons coming from the top (bottom) lead—see Fig. 1. All the quantities in Eqs. (1)–(2)—and below in Eqs. (3)–(5)—are functions of a single energy E , since we are assuming only elastic scattering mechanisms.

Starting from the entries of the scattering matrix, we introduce the following reflection $\rho_{\text{r}}, \rho_{\text{r}'}$ and transmission $\rho_{\text{t}}, \rho_{\text{t}'}$ probability matrices:

$$\begin{aligned} \rho_{\text{r}} &\equiv \mathbb{r}\mathbb{r}^\dagger, & \rho_{\text{r}'} &\equiv \mathbb{r}'(\mathbb{r}')^\dagger \\ \rho_{\text{t}} &\equiv \mathbb{t}\mathbb{t}^\dagger, & \rho_{\text{t}'} &\equiv \mathbb{t}'(\mathbb{t}')^\dagger. \end{aligned} \quad (3)$$

Here, $\mathbb{r}, \mathbb{r}', \mathbb{t}$, and \mathbb{t}' are matrices in spin space with matrix elements $r_{\sigma,\sigma'}, r'_{\sigma,\sigma'}, t_{\sigma,\sigma'}, t'_{\sigma,\sigma'}$, respectively.

We also define the following dimensionless spin conductances [44] for each scattering process:

$$\begin{aligned} \sigma_{\text{r}} &\equiv \text{Tr}[\hat{s}_z \rho_{\text{r}}], & \sigma_{\text{r}'} &\equiv \text{Tr}[\hat{s}_z \rho_{\text{r}'}] \\ \sigma_{\text{t}} &\equiv \text{Tr}[\hat{s}_z \rho_{\text{t}}], & \sigma_{\text{t}'} &\equiv \text{Tr}[\hat{s}_z \rho_{\text{t}'}]. \end{aligned} \quad (4)$$

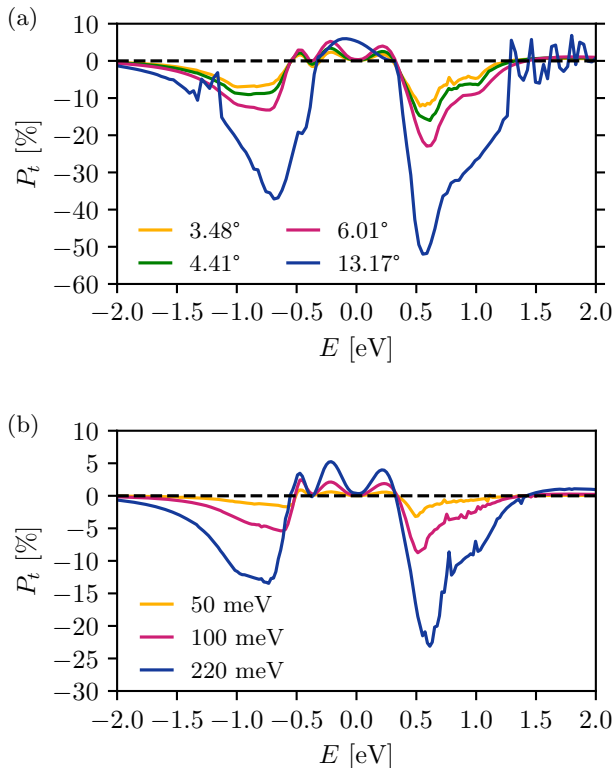


FIG. 3. (Color online) Panel (a) Results for the spin polarization $P_t(E)$ for different values of the twist angle θ ($\theta = 3.48^\circ, 4.41^\circ, 6.01^\circ$, and 13.17°). The black dashed line refers to the non-chiral $\theta = 0$ case. Panel (b) Results for the spin polarization $P_t(E)$ for different values of λ_0 ($\lambda_0 = 50$ meV, 100 meV, and 220 meV). In this panel, the angle has been fixed at $\theta = 6.01^\circ$. The black dashed line refers to the case in which SOC is artificially turned off by setting $\lambda_0 = 0$. All the other parameters are the same as in Fig. 2.

where \hat{s}_z is a Pauli matrix. The trace operation in Eq. (4) is of course intended over the spin degrees of freedom.

Once again, as demonstrated in great detail in Ref. [42], the reciprocity theorem [41] allows one to conclude that any linear-response electrical measurement in a two-terminal setup, even in the presence of auxiliary

ferromagnets, is *insensitive* to the “spin conductances” introduced in Eq. (4). The setup depicted in Fig. 1 therefore should not be intended as a real experimental setup to infer information on the quantities in Eq. (4), but, rather, as a computational setup with asymptotic propagating states to numerically access the full scattering matrix.

The four quantities in Eq. (4) are not independent. Because of charge conservation (i.e. because of the unitarity of the full scattering matrix), $\sigma_r = -\sigma_{r'}$ and $\sigma_{r'} = -\sigma_t$. Therefore, in general, we have two independent spin conductances, e.g. σ_t and $\sigma_{t'}$. From now on, we focus only on σ_t for reasons that will become clear momentarily. In particular, we introduce the energy-dependent *chirality-induced spin polarization* $P_t(E)$ by properly normalizing the corresponding spin conductance:

$$P_t(E) \equiv \frac{\sigma_t(E)}{\text{Tr}[\rho_{\mathbb{k}}(E)]} \in [-1, 1]. \quad (5)$$

This quantity gives information on the strength of the CISS effect [42, 44] and vanishes when the scatterer is non-chiral.

Microscopic modelling of the scatterer.—For what concerns the microscopic modelling of the scatterer, i.e. the twisted homobilayer TMD, we employed a gapped Dirac-fermion model [32], by introducing a mass term in a tight-binding Hamiltonian for TBG [47, 48]. The details of the complete tight-binding Hamiltonian are reported in Sect. I of the Supplemental Material [49]. Here, given its crucial importance, we focus only on the tight-binding description of SOC in twisted homobilayer TMDs. Among all the possible SOC terms allowed by C_3 symmetry [50], we restrict our analysis to *spin-flipping* nearest-neighbor intra-layer hoppings, since nearest-neighbour and next-nearest-neighbour *spin-conserving* hopping terms yield a vanishing contribution to the CISS strength (5). The fact that the physics of CISS requires, at a general, fundamental level, spin-flip processes is in agreement with the conclusions of Ref. [42].

The SOC Hamiltonian we consider here is then given by [50]:

$$\hat{\mathcal{H}}_{\text{SOC}}^{(\ell)} = \frac{2i}{3} \lambda_0^{(\ell)} \sum_{\sigma \neq \sigma'} \sum_{\langle m, n \rangle} \sum_{\tau, \tau'} [\hat{\mathbf{s}} \times \mathbf{d}_{m, \tau, n, \tau'}]_{\sigma, \sigma'} |m, \ell, \tau\rangle \langle n, \ell, \tau'| \otimes |\sigma\rangle \langle \sigma'|, \quad (6)$$

where $\ell = 1, 2$ is the layer index, $\lambda_0^{(\ell)} = [\lambda_0 - (-1)^\ell \lambda_{\text{BR}}]$ is the SOC parameter (with units of energy), $\hat{\mathbf{s}} = (\hat{s}_x, \hat{s}_y, \hat{s}_z)$ is a vector of Pauli matrices, $|m, \ell, \tau\rangle \otimes |\sigma\rangle$ denotes the state of an electron with spin σ localized on site m and sublattice $\tau = A, B$ of layer ℓ (for further details,

see Ref. [49]). Finally, $\mathbf{d}_{m, \tau, n, \tau'}$ is a dimensionless unit vector lying in the \hat{x} - \hat{y} plane, which points from lattice site n to the nearest-neighbor site m . The symbol $\langle \dots \rangle$ in one of the sums in Eq. (6) refers to the fact that the sum is restricted to nearest-neighbor pairs. One important

observation is now in order. The SOC parameter λ_0 is an intrinsic intra-layer term—intrinsic in the sense that it is also present in Bernal-stacked bilayer graphene [51]. The layer-dependent term, controlled by λ_{BR} , stems instead from broken inversion symmetry. This latter term, which, in an ordinary Bernal-stacked bilayer graphene is due to a perpendicular applied electric field [51], here models the fact that twisted homobilayer TMDs do not have an inversion center, even in the absence of extrinsic external electric fields. Finally, we note that, in the case $\lambda_{\text{BR}} = 0$, our setup is invariant under the simultaneous exchange of a) top and bottom leads and b) top and bottom layers of the twisted homobilayer TMD. In this case, one has $\sigma_{t'} = -\sigma_t$. For $\lambda_{\text{BR}} \neq 0$, $\sigma_{t'} \neq -\sigma_t$.

While certainly approximate, this lightweight model of the scatterer treats on equal footing the structural chirality of the system (i.e. which stems from the non-zero twist angle θ contained in the intra- and inter-layer terms of the twisted TMD Hamiltonian reported in Ref. [49]) and the coupling between spin and orbital motion due the SOC term of the Hamiltonian, allowing us to perform a first exploration of their interplay in a chiral quasi-2D solid-state system.

Results.—We now present our main numerical results. We used the Kwant software package [52] to implement the tight-binding model Hamiltonian introduced above and calculate the spin-resolved $S_{\sigma,\sigma'}$ matrix of the two-terminal 3D transport setup presented in Fig. 1. Top and bottom leads are modelled as semi-infinite A-A stacked graphite leads. Each graphite lead is rotated in order to be aligned with the adjacent layer belonging to the twisted homobilayer TMD. The leads have Bloch translational invariance both along the \hat{x} - \hat{y} plane and the \hat{z} direction. The twisted homobilayer TMD has Bloch translational invariance in the \hat{x} - \hat{y} plane. The spin-resolved scattering matrix $S_{\sigma,\sigma'}$ has been computed by carrying out integrals over the 2D moiré lattice Brillouin zone.

Fig. 2 displays the spin polarization $P_t(E)$, as defined in Eq. (5), of the electrons transmitted from the top to the bottom lead. These results refer to twisted homobilayer MoTe_2 [32] and a twist angle $\theta = 6.01^\circ$. (Additional numerical results for twisted MoS_2 , MoSe_2 , WS_2 , WSe_2 , and WTe_2 are reported in Sect. II of Ref. [49].) For the SOC parameters, we have used the values $\lambda_0 = 220$ meV and $\lambda_{\text{BR}} = 0$, which have been taken from Ref. [32]. We clearly see that the spin polarization exceeds 20% (see also Fig. 3(a), where much larger values have been obtained for larger twist angles), which is a giant value, given the atomic thickness of the scatterer. As expected, the calculated spin polarization has opposite sign for two opposite twist angles, θ and $-\theta$. Importantly, the spin polarization vanishes in the non-chiral $\theta = 0$ case.

The dependence of the chirality-induced spin polarization $P_t(E)$ on the twist angle θ is displayed in Fig. 3(a) for three values of θ . Notice that decreasing θ , from $\theta = 13.17^\circ$ down to $\theta = 3.48^\circ$, $|P_t(E)|$ decreases. This

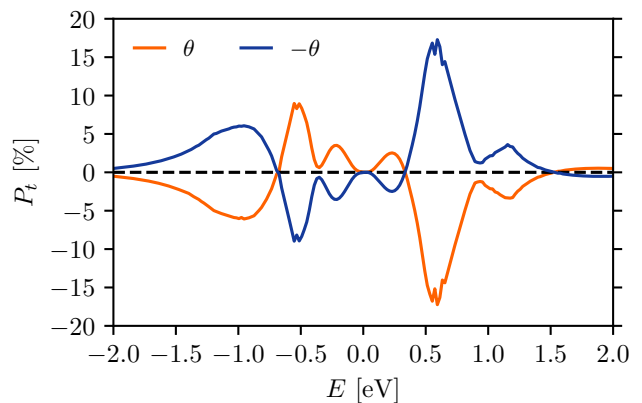


FIG. 4. (Color online) Same as in Fig. 2, but for a finite value of λ_{BR} , $\lambda_{\text{BR}} = 50$ meV. The black dashed line denotes the results for the non-chiral $\theta = 0$ case.

is not surprising since in the limit $\theta \rightarrow 0$ the system becomes non-chiral and $P_t(E)$ vanishes for all values of E , as seen in Fig. 2. For $\theta = 13.17^\circ$, the spin polarization nearly reaches the impressive value of 60%. Fig. 3(b) shows the dependence of $P_t(E)$ on the magnitude of λ_0 (while keeping $\lambda_{\text{BR}} = 0$). We note that increasing SOC leads to an overall increase of $|P_t(E)|$, pointing out the crucial role of this term in the twisted homobilayer TMD Hamiltonian for the emergence of chirality-induced spin polarization.

Finally, Fig. 4 shows $P_t(E)$ in the case of finite λ_{BR} . The important thing to notice is the result for $\theta = 0$, i.e. $P_t(E) = 0 \forall E$. At $\theta = 0$ and $\lambda_{\text{BR}} \neq 0$, our twisted quasi-2D material reduces to a Bernal-stacked homobilayer TMD in the presence of a perpendicular applied electric field. The Hamiltonian of this system breaks inversion symmetry but lacks chirality, yielding *no* chirality-induced spin polarization.

In summary, we have shown that a chirality-induced spin polarization emerges in moiré materials with strong spin-orbit coupling. Surprisingly, we have found that the spin polarization can be giant even for just two twisted monolayers. We have presented a theory of the effect based on the microscopic Hamiltonian of twisted homobilayer transition metal dichalcogenides [32]. Numerical results have been obtained for twisted MoTe_2 . In this particular case, the effect appears to be gigantic, provided that the twist angle is sufficiently large. As far as the experimental detection of the effect is concerned, one needs either to employ devices with more than two terminals [42] or transcend the linear-response regime [46] (if one insists on using a two-terminal setup).

During the preparation of this manuscript, we learned about a recent theoretical work reporting chirality-induced spin polarization in bulk (three-dimensional) inorganic crystals with homochiral crystal structures, such as tellurium and transition metal disilicide com-

pounds [53].

Acknowledgements.—This work was partially supported by the European Union’s Horizon 2020 research and innovation programme under the Marie Skłodowska-Curie grant agreement No. 873028 - HYDROTRONICS and the FET project QUEFORMAL (Contract No. 829035). M.P., F.T. and G.I. acknowledge support by the MUR through the following PRIN projects: Project “q-LIMA” (Contract. No. 2020JLZ52N), Project “NETheQS” (Contract No. 2022B9P8LN), and Project “FIVE2D” (Project No. 2017SRYEJH001). F.T. also acknowledges support by the Royal Society through the International Exchanges Scheme between the UK and Italy (Grant No. IEC R2 192166). P.J.H. acknowledges support by the Gordon and Betty Moore Foundation’s EPiQS Initiative through grant GBMF9463, the Fundación Ramon Areces, and the ICFO Distinguished Visiting Professor program. F.H.L.K. acknowledges financial support from the ERC TOPONANOP (726001), the Government of Catalonia through the SGR grant, the Spanish Ministry of Economy and Competitiveness through the Severo Ochoa Programme for Centres of Excellence in R&D (Ref. SEV-2015-0522) and Explora Ciencia (Ref. FIS2017- 91599-EXP), Fundacio Cellex Barcelona, Generalitat de Catalunya through the CERCA program, the Mineco grant Plan Nacional (Ref. FIS2016-81044-P), and the Agency for Management of University and Research Grants (AGAUR) (Ref. 2017-SGR-1656).

We thank P. Novelli and B. van Wees for useful discussions and correspondence.

Computational resources have been provided by *computing@unipi*, a computing service provided by University of Pisa.

G. M., L. C., and L. L. and contributed equally to this work.

-
- [1] Ray, K., Ananthavel, S. P., Waldeck, D. H. & Naaman, R. Asymmetric scattering of polarized electrons by organized organic films of chiral molecules. *Science* **283**, 814 (1999).
- [2] Naaman, R. & Waldeck, D. H. Chiral-induced spin selectivity effect. *J. Phys. Chem. Lett.* **3**, 2178 (2012).
- [3] Naaman, R. & Waldeck, D. H. Spintronics and chirality: spin selectivity in electron transport through chiral molecules. *Annu. Rev. Phys. Chem.* **66**, 263 (2015).
- [4] Naaman, R., Paltiel, Y. & Waldeck, D. H. Chiral molecules and the electron spin. *Nat. Rev. Chem.* **3**, 250 (2019).
- [5] Naaman, R., Paltiel, Y. & Waldeck, D. H. Chiral molecules and the spin selectivity effect. *J. Phys. Chem. Lett.* **11**, 3660 (2020).
- [6] Yang, S. H., Naaman, R., Paltiel, Y. & Parkin, S. S. P. Chiral spintronics. *Nat. Rev. Phys.* **3**, 328 (2021).
- [7] Rosenberg, R. A., Abu Haija, M. & Ryan, P. J. Chiral-selective chemistry induced by spin-polarized secondary electrons from a magnetic substrate. *Phys. Rev. Lett.* **101**, 178301 (2008).
- [8] Waldeck, D. H., Naaman, R. & Paltiel, Y. The spin selectivity effect in chiral materials. *APL Mater.* **9**, 040902 (2021).
- [9] Shiota, K., Inui, A., Hosaka Y., Amano, R., Ōnuki, Y., Hedo, M., Nakama, T., Hirobe, D., Ohe, J., Kishine, J., Yamamoto, Y. M., Shishido, H. & Togawa, Y. Chirality-induced spin polarization over macroscopic distances in chiral disilicide crystals. *Phys. Rev. Lett.* **127**, 126602 (2021).
- [10] Evers, F., Aharony, A., Bar-Gill, N., Entin-Wohlman, O., Hedegård, P., Hod, O., Jelinek, P., Kamieniarz, G., Lemeshko, M., Michaeli, K., Mujica, V., Naaman, R., Paltiel, Y., Refaely-Abramson, S., Tal, O., Thijssen, J., Thoss, M., van Ruitenbeek, J. M., Venkataraman, L., Waldeck, D. H., Yan, B. & Kronik, L. Theory of chirality induced spin selectivity: progress and challenges. *Adv. Mater.* **34**, 2106629 (2022).
- [11] Liu, Y., Xiao, J., Koo, J. & Yan, B. Chirality-driven topological electronic structure of DNA-like materials. *Nat. Mater.* **20**, 638 (2021).
- [12] Fransson, J. Chirality-induced spin selectivity: the role of electron correlations. *J. Phys. Chem. Lett.* **10**, 7126 (2019).
- [13] Fransson, J. Vibrational origin of exchange splitting and “chiral-induced spin selectivity”. *Phys. Rev. B* **102**, 235416 (2020).
- [14] Volosniev, A. G., Alpern, H., Paltiel, Y., Millo, O., Lemeshko, M. & Ghazaryan, A. Interplay between friction and spin-orbit coupling as a source of spin polarization. *Phys. Rev. B* **104**, 024430 (2021).
- [15] Andrei, E. Y. & MacDonald, A. H. Graphene bilayers with a twist. *Nat. Mater.* **19**, 1265 (2020).
- [16] Andrei, E. Y., Efetov, D. K., Jarillo-Herrero, P., MacDonald, A. H., Mak, K. F., Senthil, T., Tutuc, E., Yazdani, A. & Young, A. F. The marvels of moiré materials. *Nat. Rev. Mater.* **6**, 201 (2021).
- [17] Kennes, D. M., Claassen, M., Xian, L., Georges, A., Millis, A. J., Hone, J., Dean, C. R., Basov, D. N., Pasupathy, A. & Rubio, A. Moiré heterostructures as a condensed-matter quantum simulator. *Nat. Phys.* **17**, 155 (2021).
- [18] Cao, Y., Fatemi, V., Fang, S., Watanabe, K., Taniguchi, T., Kaxiras, E. & Jarillo-Herrero, P. Unconventional superconductivity in magic-angle graphene superlattices. *Nature* **556**, 43 (2018).
- [19] Cao, Y., Fatemi, V., Demir, A., Fang, S., Tomarken, S. L., Luo, J. Y., Sanchez-Yamagishi, J. D., Watanabe, K., Taniguchi, T., Kaxiras, E., Ashoori, R. C. & Jarillo-Herrero, P. Correlated insulator behaviour at half-filling in magic-angle graphene superlattices. *Nature* **556**, 80 (2018).
- [20] Lopes dos Santos, J. M. B., Peres, N. M. R. & Castro Neto, A. H. Graphene bilayer with a twist: electronic structure. *Phys. Rev. Lett.* **99**, 256802 (2007).
- [21] Shallcross, S., Sharma, S. & Pankratov, O. A. Quantum interference at the twist boundary in graphene. *Phys. Rev. Lett.* **101**, 056803 (2008).
- [22] Mele, E. J., Commensuration and interlayer coherence in twisted bilayer graphene. *Phys. Rev. B* **81**, 161405(R) (2010).
- [23] Li, G., Luican, A., Lopes dos Santos, J. M. B., Castro Neto, A. H., Reina, A., Kong, J. & Andrei, E. Y. Observation of Van Hove singularities in twisted graphene

- layers. *Nat. Phys.* **6**, 109 (2010).
- [24] Shallcross, S., Sharma, S., Kandelaki, E. & Pankratov, O. A. Electronic structure of turbostratic graphene. *Phys. Rev. B* **81**, 165105 (2010).
- [25] Suárez Morell, E., Correa, J. D., Vargas, P., Pacheco, M. & Barticevic, Z. Flat bands in slightly twisted bilayer graphene: tight-binding calculations. *Phys. Rev. B* **82**, 121407(R) (2010).
- [26] Bistrizter R. & MacDonald, A. H. Transport between twisted graphene layers. *Phys. Rev. B* **81**, 245412 (2010).
- [27] Bistrizter, R. & MacDonald, A. H. Moiré bands in twisted double-layer graphene. *Proc. Natl. Acad. Sci. (USA)* **108**, 12233 (2011).
- [28] Lopes dos Santos, J. M. B., Peres, N. M. R. & Castro Neto, A. H. Continuum model of the twisted graphene bilayer. *Phys. Rev. B* **86**, 155449 (2012).
- [29] Landau, L. D. & Lifshitz, E. M. *Course of Theoretical Physics: Electrodynamics of Continuous Media* (Pergamon Press, New York, 1984).
- [30] Kim, C. J., Sánchez-Castillo, A., Ziegler, Z., Ogawa, Y., Noguez, C. & Park, J. Chiral atomically thin films. *Nat. Nanotech.* **11**, 520 (2016).
- [31] Suárez Morell, E., Chico, L. & Brey, L. Twisting dirac fermions: circular dichroism in bilayer graphene. *2D Mater.* **4**, 035015 (2017).
- [32] Wu, F., Lovorn, T., Tutuc, E., Martin, I. & MacDonald, A. H. Topological insulators in twisted transition metal dichalcogenide homobilayers. *Phys. Rev. Lett.* **122**, 086402 (2019).
- [33] Cai, J., Anderson, E., Wang, C., Zhang, C., Liu, X., Holtzmann, W., Zhang, Y., Fan, F., Taniguchi, T., Watanabe, K., Ran, Y., Cao, T., Fu, L., Xiao, D., Yao, W. & Xu, X. Signatures of fractional quantum anomalous Hall states in twisted MoTe₂. *Nature* **622**, 63 (2023).
- [34] Park, H., Cai, J., Anderson, E., Zhang, Y., Zhu, J., Liu, X., Wang, C., Holtzmann, W., Hu, C., Liu, Z., Taniguchi, T., Watanabe, K., Chu, J.-H., Cao, T., Fu, L., Yao, W., Chang, C.-Z., Cobden, D., Xiao, D. & Xu, X. Observation of fractionally quantized anomalous Hall effect. *Nature* **622**, 74 (2023).
- [35] Zeng, Y., Xia, Z., Kang, K., Zhu, J., Knüppel, P., Vaswani, C., Watanabe, K., Taniguchi, T., Mak, K. F. & Shan, J. Thermodynamic evidence of fractional Chern insulator in moiré MoTe₂. *Nature* **622**, 69 (2023).
- [36] Xu, F., Sun, Z., Jia, T., Liu, C., Xu, C., Li, C., Gu, Y., Watanabe, K., Taniguchi, T., Tong, B., Jia, J., Shi, Z., Jiang, S., Zhang, Y., Liu, X. & Li, T. Observation of integer and fractional quantum anomalous Hall effects in twisted bilayer MoTe₂. *Phys. Rev. X* **13**, 031037 (2023).
- [37] Naaman, R., Waldeck, D. H. & Fransson, J. New perspective on electron transfer through molecules. *J. Phys. Chem. Lett.* **13**, 11753 (2022).
- [38] Provost, J. P. & Vallee, G. Riemannian structure on manifolds of quantum states, *Comm. Math. Phys.* **76**, 289 (1980).
- [39] Xiao, D., Chang, M. C. & Niu, Q. Berry phase effects on electronic properties. *Rev. Mod. Phys.* **82**, 1959 (2010).
- [40] Törmä, P., Peotta, S. & Bernevig, B. A. Superconductivity, superfluidity and quantum geometry in twisted multilayer systems. *Nat. Rev. Phys.* **4**, 528 (2022).
- [41] Büttiker, M. Symmetry of electrical conduction. *IBM J. Res. Dev.* **32**, 317 (1988).
- [42] Yang, X., van der Wal, C. H. & van Wees, B. J. Spin-dependent electron transmission model for chiral molecules in mesoscopic devices. *Phys. Rev. B* **99**, 024418 (2019).
- [43] Nazarov, Y. V. & Blanter, Y. M. *Quantum Transport*, (Cambridge University Press, 2012).
- [44] Wolf, Y., Liu, Y., Xiao, J., Park, N. & Yan, B. Unusual spin polarization in the chirality-induced spin selectivity. *ACS Nano* **16**, 18601 (2022).
- [45] Xiao, J., Zhao, Y. & Yan, B. Nonreciprocal nature and induced tunneling barrier modulation in chiral molecular devices. Preprint at <https://doi.org/10.48550/arXiv.2201.03623>.
- [46] A powerful, general approach to spin and charge transport through any (non-magnetic) chiral system has been proposed in Ref. [42] and by the authors of the following works: Yang, X., van der Wal, C. H. & van Wees, B. J. Detecting chirality in two-terminal electronic nanodevices. *Nano Lett.* **20**, 6148 (2020) and Yang, X. & van Wees, B. J., Linear-response magnetoresistance effects in chiral systems *Phys. Rev. B* **104**, 155420 (2021). In the framework of such phenomenological approach one can include for example dephasing and spin relaxation. Our aim, however, is to present quantitative numerical predictions for twisted 2D materials and this is why we have used the standard spin-resolved scattering matrix approach based on microscopic Hamiltonians.
- [47] de Laissardière, G. T., Mayou, D. & Magaud, L. Numerical studies of confined states in rotated bilayers of graphene. *Phys. Rev. B* **86**, 125413 (2012).
- [48] dos Santos, J. M. B. L., Peres, N. M. R. & Neto, A. H. C. Continuum model of the twisted graphene bilayer. *Phys. Rev. B* **86**, 155449 (2012).
- [49] See the Supplemental Material file for additional details on the derivation of the tight-binding Hamiltonian and further numerical results.
- [50] Kochan, D., Irmer, S. & Fabian, J. Model spin-orbit coupling Hamiltonians for graphene systems. *Phys. Rev. B* **95**, 165415 (2017).
- [51] Kunschuh, S., Gmitra, M., Kochan, D. & Fabian, J. Theory of spin-orbit coupling in bilayer graphene. *Phys. Rev. B* **85**, 115423 (2012).
- [52] Groth, C. W., Wimmer, M., Akhmerov, A. R. & Waintal, X. Kwant: a software package for quantum transport. *New J. Phys.* **16**, 063065 (2014).
- [53] Yang, Q., Li, Y., Felser, C. & Yan, B. Chirality induced spin selectivity in chiral crystals. Preprint at <https://doi.org/10.48550/arXiv.2312.04366>.

Supplemental Material for: “Chirality-Induced Spin Polarization in Twisted Bilayer Transition Metal Dichalcogenides”

Guido Menichetti,¹ Lorenzo Cavicchi,² Leonardo Lucchesi,^{1,3} Fabio Taddei,^{4,2} Giuseppe Iannaccone,³ Pablo Jarillo-Herrero,⁵ Claudia Felser,⁶ Frank H. L. Koppens,^{7,8} Marco Polini^{1,7}

¹*Dipartimento di Fisica dell’Università di Pisa, Largo Bruno Pontecorvo 3, I-56127 Pisa, Italy*

²*Dipartimento di Ingegneria dell’Informazione dell’Università di Pisa, Via Girolamo Caruso 16, I-56122 Pisa, Italy*

³*Scuola Normale Superiore, Piazza dei Cavalieri 7, I-56126 Pisa, Italy*

⁴*NEST, Istituto Nanoscienze-CNR, Piazza S. Silvestro 12, I-56126 Pisa, Italy*

⁵*Department of Physics, Massachusetts Institute of Technology, Cambridge, Massachusetts, USA*

⁶*Max Planck Institute for Chemical Physics of Solids, Nöthnitzer Str. 40, Dresden 01187, Germany*

⁷*ICFO-Institut de Ciències Fotòniques, The Barcelona Institute of Science and Technology, Av. Carl Friedrich Gauss 3, 08860 Castelldefels (Barcelona), Spain*

⁸*ICREA-Institució Catalana de Recerca i Estudis Avançats, Passeig de Lluís Companys 23, 08010 Barcelona, Spain*

In this Supplemental Material we present more details on the tight-binding Hamiltonian we have used in our numerical calculations. We also present further numerical results concerning the chirality-induced spin-polarization for two of the most common families of TMDs.

SECTION I: MODEL HAMILTONIAN

Here we present more details on the tight-binding model we have used to describe electrons roaming in the twisted TMD homobilayer moiré superlattice.

We start from the tight binding model for TBG [S1–S3]. The basis of Bloch states is built from the p_z atomic orbitals of Carbon. We introduce the localized atomic orbitals centered at the point $\mathbf{d}_{\tau,\ell} + \mathbf{t}_{n,\ell}$, i.e.

$$\langle \mathbf{r} | n, \ell, \tau \rangle = \phi(\mathbf{r} - \mathbf{d}_{\tau,\ell} - \mathbf{t}_{n,\ell}), \quad (\text{S1})$$

where $\phi(\mathbf{r})$ is the wavefunction of a p_z orbital centered at the origin, $\mathbf{d}_{\tau,\ell}$ is the basis vector of the sublattice τ in layer ℓ , whereas the symbol $\mathbf{t}_{n,\ell}$ is a shorthand for

$$\mathbf{t}_{n,\ell} = n_1 \tilde{\mathbf{t}}_{1,\ell} + n_2 \tilde{\mathbf{t}}_{2,\ell} \quad \text{with } n_1, n_2 \in \mathbb{N}. \quad (\text{S2})$$

The vectors $\tilde{\mathbf{t}}_{1/2,\ell}$ are primitive translation vectors of the graphene lattice in layer ℓ , and the sum over n should be intended as

$$\sum_n [\dots] = \sum_{n_1, n_2 \in \mathbb{N}} [\dots]. \quad (\text{S3})$$

The atomic orbitals are assumed to be orthogonalized according to

$$\langle n, \ell, \tau | n', \ell', \tau' \rangle = \delta_{n,n'} \delta_{\ell,\ell'} \delta_{\tau,\tau'}. \quad (\text{S4})$$

In the two-center approximation, and retaining only the nearest-neighbour contributions, the intra-layer Hamiltonian of graphene in layer ℓ takes the form

$$\hat{H}_{\text{intra}}^{(\ell)} = -t \sum_{\langle m,n \rangle} \sum_{\tau,\tau'} |m, \ell, \tau\rangle \langle n, \ell, \tau'| (1 - \delta_{\tau,\tau'}), \quad (\text{S5})$$

where the energy t is given by

$$-t \equiv \int d\mathbf{r} \phi^*(\mathbf{r}) V(\mathbf{r} - \mathbf{d}_{\tau,1}) \phi(\mathbf{r} - \mathbf{d}_{\tau,1}) = \int d\mathbf{r} \phi^*(\mathbf{r}) V(\mathbf{r} - \mathbf{d}_{\tau,2}) \phi(\mathbf{r} - \mathbf{d}_{\tau,2}), \quad (\text{S6})$$

$V(\mathbf{r})$ being the spherically-symmetric potential of a Carbon atom centered at the origin. The sum over $\langle m, n \rangle$ runs over neighboring orbitals, i.e. the states $|m, \ell, \tau\rangle$ and $|n, \ell, \tau'\rangle$ in Eq. (S5) correspond to neighbouring orbitals.

In this work we have chosen the following primitive translation vectors

$$\tilde{\mathbf{t}}_{1/2,\ell=1} = \left(\mp \frac{a}{2}, \frac{a\sqrt{3}}{2} \right), \quad \tilde{\mathbf{t}}_{1/2,\ell=2} = \mathcal{R}(\theta) \left(\mp \frac{a}{2}, \frac{a\sqrt{3}}{2} \right), \quad (\text{S7})$$

where $\mathcal{R}(\theta)$ is the rotation matrix defined by:

$$\mathcal{R}(\theta) = \cos(\theta)\mathbb{1}_{2 \times 2} - i \sin(\theta)\sigma_y = \begin{pmatrix} \cos(\theta) & \pm \sin(\theta) \\ \sin(\theta) & \cos(\theta) \end{pmatrix}. \quad (\text{S8})$$

As in the main text, layer 1 (top) is the reference layer, while layer 2 (bottom) is counter-clockwise rotated by an angle θ . In addition, the basis vectors are

$$\mathbf{d}_{\tau,\ell} = \begin{cases} \frac{a}{\sqrt{3}} \left(-\frac{\sqrt{3}}{2}, \frac{1}{2} \right), & \text{if layer} = 1 \text{ and sub-lattice} = B. \\ -\frac{a}{\sqrt{3}} \mathcal{R}(\theta) \left(-\frac{\sqrt{3}}{2}, \frac{1}{2} \right), & \text{if layer} = 2 \text{ and sub-lattice} = A. \\ \mathbf{0}, & \text{otherwise.} \end{cases} \quad (\text{S9})$$

The choice of these translation and basis vectors is such that in the limit $\theta \rightarrow 0$ one obtains AB-stacked bilayer graphene.

We now describe the tunneling of electrons between orbitals in different layers. The inter-layer Hamiltonian can be written as

$$\hat{H}_{\text{inter}}^{(\ell,\ell')} = \sum_{n,n'} \sum_{\tau,\tau'} h_{\tau,\tau'}(\mathbf{d}_{\tau,\ell} + \mathbf{t}_{n,\ell} - \mathbf{d}_{\tau',\ell'} - \mathbf{t}_{n',\ell'}) |n,\ell,\tau\rangle \langle n',\ell',\tau'| + \text{H.c.} \quad (\text{S10})$$

An empirical form of the transfer integral between two p_z orbitals of Carbon atoms in the Slater-Koster approximation is given by [S2]:

$$h_{\tau,\tau'}(\mathbf{R}_{n,n'}) = -t \exp\left(-\frac{|\mathbf{R}_{n,n'}| - a}{\lambda}\right) \frac{|\mathbf{R}_{n,n'} \cdot \mathbf{e}_{\parallel}|^2}{|\mathbf{R}_{n,n'}|^2} + t_{\perp} \exp\left(-\frac{|\mathbf{R}_{n,n'}| - d}{\lambda}\right) \frac{|\mathbf{R}_{n,n'} \cdot \mathbf{e}_{\perp}|^2}{|\mathbf{R}_{n,n'}|^2}. \quad (\text{S11})$$

In Eq. (S11) we have introduced the short-hand notation $\mathbf{R}_{n,n'} \equiv \mathbf{d}_{\tau,\ell} + \mathbf{t}_{n,\ell} - \mathbf{d}_{\tau',\ell'} - \mathbf{t}_{n',\ell'}$, for which indeed $h_{\tau,\tau'}(\mathbf{d}_{\tau,\ell} + \mathbf{t}_{n,\ell} - \mathbf{d}_{\tau',\ell'} - \mathbf{t}_{n',\ell'}) = h_{\tau,\tau'}(\mathbf{R}_{n,n'})$. In Eq. (S11) we have also introduced the decay length λ and the inter-layer distance d . The hopping parameter t_{\perp} is given by:

$$t_{\perp} = \int d\mathbf{r} \phi^*(\mathbf{r}) V(\mathbf{r} - d\mathbf{e}_z) \phi(\mathbf{r} - d\mathbf{e}_z), \quad (\text{S12})$$

which is the transfer integral between two p_z orbitals that are one on top of the other, vertically displayed by a distance d .

In this work we study vertical transport through twisted homobilayer TMDs, whose Hamiltonian can be obtained by modifying the above tight-binding model into a twisted bilayer gapped graphene one [S4]. To this end, we reproduce the monolayer TMD energy gap Δ and carrier effective mass m^* by adding a staggered potential E_A, E_B on the sub-lattice sites and re-scaling the intra-layer nearest-neighbor hopping t , while retaining the lattice parameter of graphene a :

$$\hat{H}_{\text{intra}}^{(\ell)} = \sum_m \sum_{\tau} E_{\tau} |m,\ell,\tau\rangle \langle m,\ell,\tau| - \tilde{t} \sum_{\langle m,n \rangle} \sum_{\tau\tau'} |m,\ell,\tau\rangle \langle n,\ell,\tau'| (1 - \delta_{\tau\tau'}), \quad (\text{S13})$$

where

$$\tilde{t} = \frac{\hbar}{\sqrt{3}a} \sqrt{\frac{2\Delta}{3m^*}}. \quad (\text{S14})$$

The numerical results presented and discussed in the main text are obtained for the following choice of parameters: $a = 0.246$ nm, $\Delta = 1.1$ eV, and $m^* = 0.6 m_e$, m_e being the bare electron mass in vacuum. The inter-layer hopping energy and distance appearing in the inter-layer Hamiltonian term (S11) are instead fixed to $t_{\perp} = 0.15$ eV and $d = 0.69$ nm, while the exponential decay length is kept equal to the one in TBG, i.e. $\lambda = 0.184\sqrt{3}a$ [S2]. These parameters have been chosen in order to effectively reproduce the energy bands of twisted MoTe₂.

In Fig. S1 we compare our results for the energy bands obtained from the above described tight-binding model—panel (a)—with the results of Ref. [S4], which were obtained from a continuum model Hamiltonian.

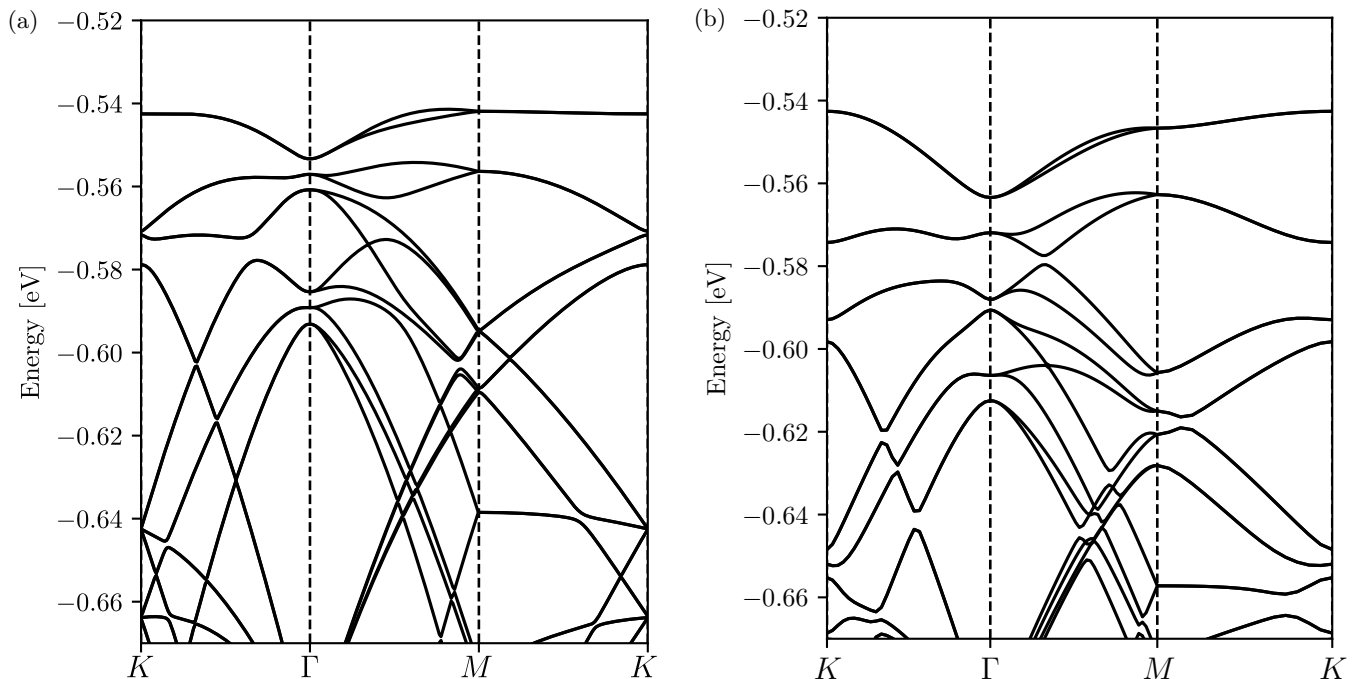


FIG. S1. Band structure of twisted MoTe₂ obtained from our tight-binding model—panel (a)—and from the continuum model of Ref. [S4]—panel (b). Results in this plot refer to a twist angle $\theta = 3.89^\circ$. The parameters of the continuum model Hamiltonian are extracted from Ref. [S4]. The dependence of the bands on the wave-vector \mathbf{k} is displayed along the high-symmetry path K - Γ - M - K of the moiré Brillouin zone.

SECTION II: ADDITIONAL NUMERICAL RESULTS

In this Section we present additional numerical results. In the main text, indeed, we focussed on for the case of twisted MoTe₂. For the sake of completeness, in Fig. S2 we show the chirality-induced spin polarization P_t for two of the most common families of TMDs. In panel (a) we report results for twisted homobilayers composed by MoS₂, MoSe₂, and MoTe₂ (already presented in the main text). In panel (b) we do the same for WS₂, WSe₂, and WTe₂. Both panels have been calculated by setting $\theta = 13.17^\circ$.

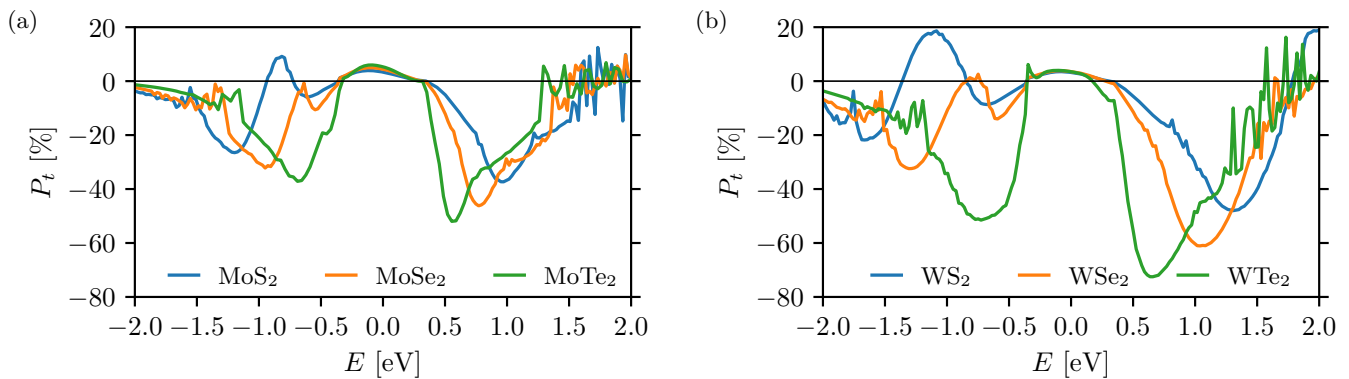


FIG. S2. (Color online) Results for the spin polarization $P_t(E)$ for two different families of twisted TMDs. Results in this figure refer to a single twist angle, i.e. $\theta = 13.17^\circ$. Panel (a) Results for MoX₂ with X = S, Se, and Te. Panel (b) Results for WX₂ with X = S, Se, and Te. In both panels the solid black line has been added as a guide to the eye. The parameters of the microscopic Hamiltonians used to produce these numerical results have been reported in Table S1.

The microscopic parameters of the Hamiltonian used to compute the spin polarization $P_t(E)$ in Fig. S2 are collected

in Table S1. Each Hamiltonian contain the following parameters: the energy gap Δ , the hole-carrier effective mass m^* (expressed in units of the bare electron mass in vacuum), the SOC parameter λ_0 discussed in the main text, and the interlayer distance d . The Table reports also the SOC to energy gap ratio λ_0/Δ and the maximum of the absolute value of the chirality-induced spin-polarization:

$$|P_t|^{\max} \equiv \max_{E \in [-2,2] \text{ eV}} |P_t(E)|, \quad (\text{S15})$$

extracted from Fig. S2. As it can be inferred from Fig. S2, within a given TMD family, $|P_t|^{\max}$ is achieved in the material with the maximum value of λ_0/Δ .

	Δ [eV]	m^* [m_e]	λ_0 [meV]	d [nm]	λ_0/Δ	$ P_t ^{\max}$ [%]
MoS ₂ [S5, S6]	1.62	0.58	255	0.62	0.16	37.3
MoSe ₂ [S5, S6]	1.4	0.67	263	0.65	0.19	46.2
MoTe ₂ [S4]	1.1	0.62	220	0.69	0.20	59.5
WS ₂ [S5, S6]	1.74	0.42	459	0.61	0.26	48.0
WSe ₂ [S5, S6]	1.43	0.45	446	0.64	0.31	61.1
WTe ₂ [S5, S6]	0.86	0.41	401	0.69	0.47	72.5

TABLE S1. Numerical parameters employed to obtain the results shown in Fig. S2. Energy gap Δ (eV), hole-carrier effective mass m^* (m_e) in units of the bare electron mass in vacuum m_e , the SOC parameter λ_0 discussed in the main text, the interlayer distance d (in nm), the SOC to energy gap ratio λ_0/Δ , and $|P_t|^{\max}$ as defined in Eq. (S15). This last quantity has been extracted from Fig. S2 and refers to $\theta = 13.17^\circ$.

In order to illustrate the role of the energy gap Δ on the quantity $P_t(E)$, in Fig. S3 we plot three different results for $P_t(E)$ in MoTe₂. Different curves in this figure have been obtained by artificially changing the energy gap Δ while keeping fixed all the other microscopic parameters of MoTe₂. The twist angle is fixed at $\theta = 6.01^\circ$. It is evident that $|P_t|^{\max}$ increases with decreasing Δ (thereby increasing the value of the ratio λ_0/Δ).

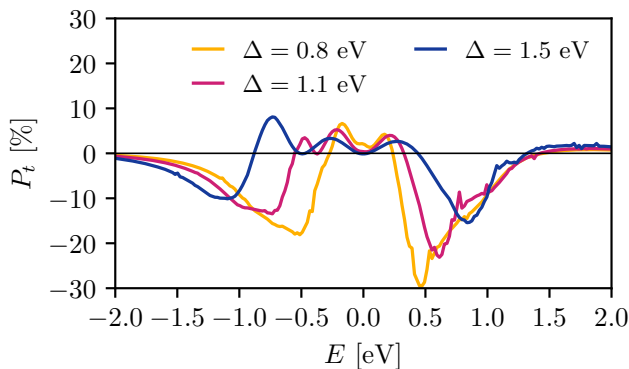


FIG. S3. (Color online) Chirality-induced spin polarization $P_t(E)$ in MoTe₂. Different colors refer to different values of Δ : $\Delta = 0.8$ eV (orange), $\Delta = 1.1$ eV (magenta), and $\Delta = 1.5$ eV (blue). All the results have been obtained by setting $\theta = 6.01^\circ$.

We conclude this Section by showing the dependence of $|P_t|^{\max}$ on the twist angle θ in Fig. S4. Results in this plot refer to twisted MoTe₂. For the computed angles, a linear behavior is evident.

-
- [S1] Lopes dos Santos, J. M. B., Peres, N. M. R. & Castro Neto, A. H. Graphene bilayer with a twist: electronic structure. *Phys. Rev. Lett.* **99**, 256802 (2007).
- [S2] de Laissardière, G. T., Mayou, D. & Magaud L. Numerical studies of confined states in rotated bilayers of graphene. *Phys. Rev. B* **86**, 125413 (2012).
- [S3] Novelli, P., Torre, I., Koppens, F. H. L., Taddei, F. & Polini, M. Optical and plasmonic properties of twisted bilayer graphene: Impact of interlayer tunneling asymmetry and ground-state charge inhomogeneity. *Phys. Rev. B* **102**, 125403 (2020).

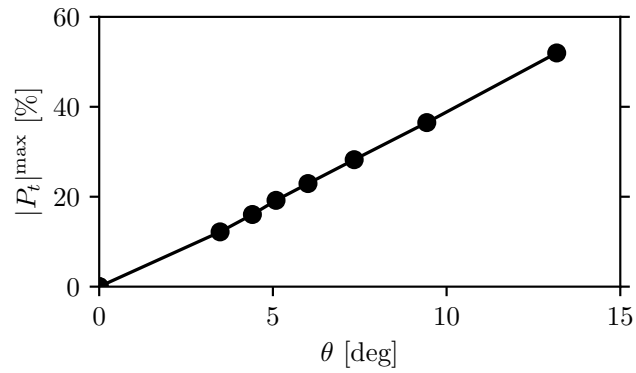


FIG. S4. The quantity $|P_t|^{\max}$ is plotted as a function of the twist angle θ . The black solid line is a guide to the eye. All the other parameters are the same as in Fig. 2 in the main text.

- [S4] Wu, F., Lovorn, T., Tutuc, E., Martin, I. & MacDonald, A. H. Topological insulators in twisted transition metal dichalcogenide homobilayers. *Phys. Rev. Lett.* **122**, 086402 (2019).
- [S5] Zibouche, N., Kuc, A., Musfeldt, J. & Heine, T. Transition-metal dichalcogenides for spintronic applications. *Ann. Phys. (Berlin)* **526**, 395 (2014).
- [S6] Kim, H.-G. & Choi, H. J. Thickness dependence of work function, ionization energy, and electron affinity of Mo and W dichalcogenides from DFT and GW calculations. *Phys. Rev. B* **103**, 085404 (2021).